Ocean Engineering 38 (2011) 409–418

Contents lists available at ScienceDirect

Ocean Engineering

journal homepage: www.elsevier.com/locate/oceaneng

Water wave interaction with surface-piercing porous cylinders using the null-field integral equations

J.T. Chen [a,b,*], Y.J. Lin [a], Y.T. Lee [a], C.F. Wu [a]

[a] Department of Harbor and River Engineering, National Taiwan Ocean University, Keelung, Taiwan
[b] Department of Mechanical and Mechatronics Engineering, National Taiwan Ocean University, Keelung, Taiwan

ARTICLE INFO

Article history:
Received 23 May 2009
Accepted 13 November 2010
Editor-in-Chief: A.I. Incecik
Available online 31 December 2010

Keywords:
Addition theorem
Null-field integral equation
Fourier series
Trapped mode
Porous cylinder
Water wave

ABSTRACT

Following the successful experiences of solving water wave scattering problems for multiple impermeable cylinders by the authors' group, we extend the null-field integral formulation in conjunction with the addition theorem and the Fourier series to deal with the problems of surface-piercing porous cylinders in this paper. In the implementation, the null-field point can be exactly located on the real boundary free of calculating the Cauchy and Hadamard principal values, thanks to the introduction of degenerate kernels (or separable kernels) for fundamental solutions. This method is a semi-analytical approach, since errors attribute from the truncation of the Fourier series. Not only a systematic approach is proposed but also the effect on the near-trapped modes due to porous cylinders and disorder of layout is examined. Several advantages such as mesh-free generation, well-posed model, principal value free, elimination of boundary-layer effect and exponential convergence, over the conventional boundary element method (BEM) are achieved. It is found that the disorder has more influence to suppress the occurrence of near-trapped modes than the porosity. The free-surface elevation is consistent with the results of William and Li and those using the conventional BEM. Besides, the numerical results of the force on the surface of cylinders agree well with those of William and Li. Besides, the present method is a semi-analytical approach for problems containing circular and elliptical shapes at the same time.

1. Introduction

Taiwan is surrounded by sea. Marine recreation activity and the exploitation of marine resources become important issues. In offshore engineering, more and more structures are built such as sheltered platform. The analysis of determining the wave loading exerted upon platform legs is necessary, and how to design a safe platform is a significant issue. Interaction of water wave impinging an array of bottom mounted cylinders of a sea platform is our main concern in this paper.

In the literature, an analytical solution for an incident water wave impinging a circular cylinder was derived by MacCamy and Fuchs (1954). By the similar way, an extension work for two cylinders was presented by Spring and Monkmeyer (1974). A semi-analytical solution using the wave function expansion was obtained for the diffraction of linear waves by arrays of cylinders. For more than one or two bodies, McIver and Evans (1984) used an approximate method to estimate the wave forces for a group of two, three and five cylinders. The method was developed by a large spacing approximation, but good results were given even when the spacing is small. Later, Linton and Evans (1990) studied the interaction of water waves with arrays of circular cylinders in a similar way to Twersky approach (1952) which was developed by employing the multipole wave expansion and the addition theorem. Linton and Evans (1990) extended this approach to calculate the force in a more neat form.

For general geometry case, we always resort to the numerical methods. Au and Brebbia (1983) employed the boundary element method (BEM) to calculate the resultant force using constant, linear and quadratic elements. In their work, not only a circular case but also a square and an elliptic one are implemented. Eatock Taylor and Hung (1985) found that the force tend to the one on an isolated cylinder multiplied by the square of the number of cylinders at low frequencies. By descretizing the boundary in a more genius way, Zhu and Moule (1996) obtained a more accurate result. However, in the previous works, they are not discussed on the issue of near-trapped mode.

Near-trapped mode means a localized behavior that energy is trapped in a truncated periodical structure. A trapped mode is associated with a singularity that lies on the real axis. Water wave diffraction and near-trapped mode by a multi-column structure were studied by Evans and Porter (1997). The wave number to excite the near-trapped modes for cases of four, five and six cylinders was determined numerically by detecting the value of *ka*, which results in the maximum force. As number of cylinders increases, Maniar and Newman (1997) discovered the Dirichlet and

* Corresponding author at: Department of Harbor and River Engineering, National Taiwan Ocean University, Keelung, Taiwan. Tel.: +886 2 24622192x6177; fax: +886 2 24632375.
E-mail address: jtchen@mail.ntou.edu.tw (J.T. Chen).

0029-8018/$ - see front matter © 2010 Elsevier Ltd. All rights reserved.
doi:10.1016/j.oceaneng.2010.11.006

Neumann trapped modes of large number of cylinders (1 0 0) in an infinite domain. It was found that the peak loads approach those of infinite number of cylinders when an array is large but finite. For multiple cylinders in a channel, trapped modes were also found by Evans and Porter (1999). Mathematically speaking, the array-guided cylinders may result in non-trivial solutions of the homogeneous problem at particular values of wave number. It can be understood as eigenvectors corresponding to eigenvalues of certain differential operators on unbounded domains even though there is no characteristic length. A characteristic length in the near-trapped mode means the length bounded by the array of cylinders.

Duclos and Clèment (2004) extended to consider arrays of unevenly spaced cylinders, displaced randomly from a regular array according to a disorder parameter. They focused on two effects of this spacing irregularity, reduction of peak forces associated to trapped mode phenomena, and regularization of the transmission coefficient for waves propagating through the arrays. However, Duclos and Clèment (2004) only considered the impermeable cylinders. On the other hand, Williams and Li (2000) calculated the free-surface elevation and force for the porous cylinders. In the numerical implementation, Chen (2004) used the BEM to obtain the free-surface elevation for the porous cylinders. Nevertheless, they did not consider the disorder effect. We may wonder what happens for the near-trapped modes if we simultaneously consider the porous cylinder with a disorder. The effect of porosity parameter on the free-surface elevation, force and near-trapped modes will be examined. Also, the reduction of force in the case of near-trapped mode due to disorder is also our interest.

In this paper, the hydrodynamics of porous cylinders is studied using the null-field integral equation in conjunction with the addition theorem and the Fourier series. The present approach based on the null-field BIEM, while the singular integrals in bump contour are transformed to series sum free of principal value sense. The main difference between the present approach and the Linton–Evans method is that we use the BIE instead of the wave function expansion. It is noted that our null-field BIE is free of boundary-layer effect which always appears in the conventional BEM. The meaning of the boundary-layer effect for the boundary element method terminology means larger error of calculated quantity near the boundary which is fully different from the boundary-layer in fluid mechanics due to viscosity. The unknown coefficient here is the Fourier coefficient on the boundary instead of weighting of wave expansion for the domain. To the authors' best knowledge, three possible cases may be modeled by porous cylinder. One is the cylinder with a lot of tiny holes on the cylinder surface. Another is the moon pool for the cylinder structure. The other is porous and thin sidewalls on the cylinder. The porosity parameter has been defined by Chwang (1983) and Twu and Lin (1991). The porosity G in this model is only a non-dimensional parameter which can be seen as a complex modulus due to dissipation energy. By viewing the model as a black box, this parameter G can be turned to match the experimental data by model updating technique. The interface condition for the porous cylinder is considered as a similar idea of complex spring in the structural dynamics. Force as well as free-surface elevation were calculated and compared with others to check the validity of our method. The parameter study for the disorder and porosity on the effect of near-trapped modes will be investigated.

2. Problem statement and integral formulation

2.1. Problem statement

Irrotational motion of the inviscid and incompressible fluid is small-amplitude which is defined as velocity potential $\Phi(x,y,z,t)$

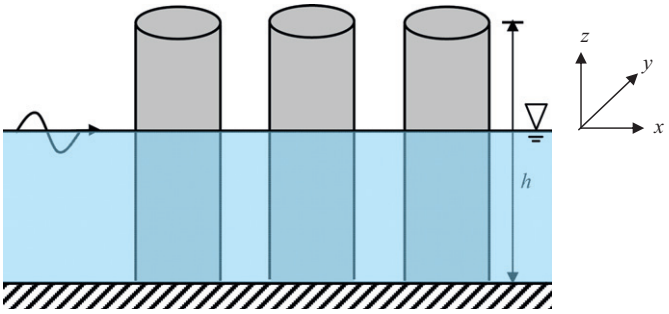

Fig. 1. Problem statement of water waves with an array of vertical cylinders.

based on the linearized water-wave theory. We assume that there are N vertical circular cylinders mounted at $z=-h$ upward to the free-surface as shown in Fig. 1. The governing equation of the water wave problem is the Laplace equation

$$\nabla^2\Phi(x,y,z,t)=0, \quad (x,y,z)\in D \tag{1}$$

where ∇^2 and D are the Laplacian operator and the domain of interest, respectively. The linearized kinematical condition on the bottom is

$$\left(\frac{\partial\Phi}{\partial z}\right)_{z=-h}=0 \tag{2}$$

and the linearized condition on the free-surface is

$$\left(-\frac{\omega^2}{g}\Phi+\frac{\partial\Phi}{\partial z}\right)_{z=0}=0 \tag{3}$$

where g is the acceleration due to gravity, ω denotes the angular frequency and h is the water depth. The velocity potential must also satisfy the kinematical conditions on the wetted surface of all bodies

$$\frac{\partial\Phi}{\partial n}=0, \quad -h\le z\le 0 \tag{4}$$

where n stands for the normal vector of anybody with respect to its local circular coordinate system. Using separation of variables for space and time, we have

$$\Phi(x,y,z,t)=u(x,y)f(z)e^{-i\omega t} \tag{5}$$

where

$$f(z)=\frac{-igA}{\omega}\frac{\cosh k(z+h)}{\cosh kh}=\frac{-igH}{2\omega}\frac{\cosh k(z+h)}{\cosh kh} \tag{6}$$

in which A is the amplitude of incident wave and equals to half of the wave height H, g is the acceleration of gravity, k is the wave number and $i^2=-1$. $\phi(x,y,t)$ can be defined by

$$\varphi(x,y,t)=\eta(x,y)e^{-i\omega t} \tag{7}$$

where $\varphi(x,y,t)$ is the free-surface elevation, in which

$$\eta(x,y)=Au(x,y) \tag{8}$$

The potential of incident wave $u_{inc}(x,y)$ is shown below:

$$u_{inc}(x,y)=e^{ik(x\cos\theta_{inc}+y\sin\theta_{inc})}\equiv e^{ik\rho\cos(\phi-\theta_{inc})} \tag{9}$$

where θ_{inc} is the angle of incident wave, $\rho=\sqrt{x^2+y^2}$ and $\phi=\arctan(y/x)$. Substituting Eq. (2) into Eq. (1) and using Eq. (3), we have

$$(\nabla^2+k^2)u(x,y)=0, \quad (x,y)\in D \tag{10}$$

The boundary conditions are shown below:

$$\frac{\partial u^O}{\partial r}=-\frac{\partial u_j^C}{\partial r}=ikG(u_j^C-u^O) \tag{11}$$

where the superscripts O and C denote the regions of ocean and cylinder, respectively, G is the dimensionless parameter of porosity

and the dispersion relationship is

$$k\tanh kh=\frac{\omega^2}{g} \tag{12}$$

The dynamic pressure can be obtained by

$$p=-\rho_{\mathrm{f}}\frac{\partial \Phi}{\partial t}=-\rho_f gA\frac{\cosh k(z+h)}{\cosh kh}u(x,y)e^{-i\omega t} \tag{13}$$

where ρ_f is the density of the fluid. The two components of the first-order force X^j on the jth cylinder are given by integrating the pressure over the circular boundary as shown below:

$$X^j=-\frac{\rho gAa_j}{k}\tanh kh\int_0^{2\pi}u(x,y)\left\{\begin{array}{c}\cos\theta_j\\ \sin\theta_j\end{array}\right\}d\theta_j \tag{14}$$

where a_j denotes the radius of the jth cylinder.

2.2. Dual integral equations—the conventional version

The boundary integral equation for the domain point can be derived from the Green's third identity (Chen et al., 2003), we have

$$2\pi u(\mathbf{x})=\int_B T(\mathbf{s},\mathbf{x})u(\mathbf{s})dB(\mathbf{s})-\int_B U(\mathbf{s},\mathbf{x})t(\mathbf{s})dB(\mathbf{s}),\quad \mathbf{x}\in D, \tag{15}$$

$$2\pi t(\mathbf{x})=\int_B M(\mathbf{s},\mathbf{x})u(\mathrm{s})dB(\mathbf{s})-\int_B L(\mathbf{s},\mathbf{x})t(\mathbf{s})dB(\mathbf{s}),\quad \mathbf{x}\in D \tag{16}$$

where $\mathbf{s}$ and $\mathbf{x}$ are the source and field points, respectively, $t(\mathbf{s})=(\partial u(\mathbf{s})/\partial n_{\mathbf{s}})$, B is the boundary, $n_{\mathbf{s}}$ denotes the outward normal vectors at the source point $\mathbf{s}$. The kernel function $U(\mathbf{s},\mathbf{x})$ is the fundamental solution which satisfies

$$(\nabla^2+k^2)U(\mathbf{s},\mathbf{x})=2\pi\delta(\mathbf{x}-\mathbf{s}) \tag{17}$$

in which $\delta(\mathbf{x}-\mathbf{s})$ denotes the Dirac–delta function. Then, we can obtain the fundamental solution as follows

$$U(\mathbf{s},\mathbf{x})=\frac{-i\pi H_0^{(1)}(kr)}{2} \tag{18}$$

where $H_0^{(1)}(kr)$ is the zeroth Hankel function of the first kind and $r\equiv|\mathbf{s}-\mathbf{x}|$. The other kernels functions, $T(\mathbf{s},\mathbf{x})$, $L(\mathbf{s},\mathbf{x})$, and $M(\mathbf{s},\mathbf{x})$, are defined by

$$T(\mathbf{s},\mathbf{x})=\frac{\partial U(\mathbf{s},\mathbf{x})}{\partial n_{\mathrm{s}}}, \tag{19}$$

$$L(\mathbf{s},\mathbf{x})=\frac{\partial U(\mathbf{s},\mathbf{x})}{\partial n_{\mathrm{x}}}, \tag{20}$$

$$M(\mathbf{s},\mathbf{x})=\frac{\partial^2 U(\mathbf{s},\mathbf{x})}{\partial n_{\mathrm{s}}\partial n_{\mathrm{x}}} \tag{21}$$

where $n_{\mathbf{x}}$ denotes the unit outward normal vector at the field point $\mathbf{x}$. By moving the field point $\mathbf{x}$ to the boundary, the dual boundary integral equations for the boundary point can be obtained as follows:

$$\pi u(\mathbf{x})=C.P.V.\int_B T(\mathbf{s},\mathbf{x})u(\mathbf{s})dB(\mathbf{s})-R.P.V.\int_B U(\mathbf{s},\mathbf{x})t(\mathrm{s})dB(\mathbf{s}),\quad \mathbf{x}\in B, \tag{22}$$

$$\pi t(\mathbf{x})=H.P.V.\int_B M(\mathbf{s},\mathbf{x})u(\mathbf{s})dB(\mathbf{s})-C.P.V.\int_B L(\mathbf{s},\mathbf{x})t(\mathbf{s})dB(\mathbf{s}),\quad \mathbf{x}\in B \tag{23}$$

where *R.P.V.*, *C.P.V.* and *H.P.V.* denote the Riemann principal value, Cauchy principal value and Hadamard (or called Mangler) principal value, respectively. By moving the field point to the complementary domain, the dual null-field integral equations are given below

$$0=\int_B T(\mathbf{s},\mathbf{x})u(\mathbf{s})dB(\mathbf{s})-\int_B U(\mathbf{s},\mathbf{x})t(\mathbf{s})dB(\mathbf{s}),\quad \mathbf{x}\in D^c, \tag{24}$$

$$0=\int_B M(\mathbf{s},\mathbf{x})u(\mathbf{s})dB(\mathbf{s})-\int_B L(\mathbf{s},\mathbf{x})t(\mathbf{s})dB(\mathbf{s}),\quad \mathbf{x}\in D^c \tag{25}$$

where D^c is the complementary domain. The region bounded by the boundary for the field solution is called the "domain". However, the region out of the domain is called the "complementary domain". Mathematically speaking, $D+D^c=$full plane. When the collocation point in the BIE is outside the domain, it results in a null response in the left-hand side of the null-field BIE as shown in Eqs. (24) and (25) Eqs. (15), (16), (24) and (25) are conventional formulations, where the point cannot be located on the real boundary. Singularity occurs and concept of principal values is required once Eqs. (22) and (23) are considered.

2.3. Dual boundary integral formulation—the present version

By introducing the degenerate kernel, the collocation point can be exactly located on the real boundary free of calculating singular integrals in the sense of principal value. The degenerate kernel can separate the field and source points for the closed-form fundamental solution. Therefore, the integral equations for the domain point and null-field integral equations in the interior problem are represented as

$$2\pi u(\mathbf{x})=\int_B T^I(\mathbf{s},\mathbf{x})u(\mathrm{s})dB(\mathbf{s})-\int_B U^I(\mathbf{s},\mathbf{x})t(\mathrm{s})dB(\mathbf{s}),\quad \mathbf{x}\in D\cup B, \tag{26}$$

$$2\pi t(\mathbf{x})=\int_B M^I(\mathbf{s},\mathbf{x})u(\mathbf{s})dB(\mathbf{s})-\int_B L^I(\mathbf{s},\mathbf{x})t(\mathbf{s})dB(\mathbf{s}),\quad \mathbf{s}\in D\cup B, \tag{27}$$

and

$$0=\int_B T^E(\mathbf{s},\mathbf{x})u(\mathbf{s})dB(\mathbf{s})-\int_B U^E(\mathbf{s},\mathbf{x})t(\mathbf{s})dB(\mathbf{s}),\quad \mathbf{x}\in D^c\cup B, \tag{28}$$

$$0=\int_B M^E(\mathbf{s},\mathbf{x})u(\mathrm{s})dB(\mathbf{s})-\int_B L^E(\mathbf{s},\mathbf{x})t(\mathbf{s})dB(\mathbf{s}),\quad \mathbf{x}\in D^c\cup B \tag{29}$$

where the superscripts I and E denote interior and exterior degenerate kernels for fundamental solutions respectively. For the exterior problem, the domain of interest is in the external region of the circular boundary and the complementary domain is in the internal region of the circle. Therefore, the null-field integral equations are represented as

$$2\pi u(\mathbf{x})=\int_B T^E(\mathbf{s},\mathbf{x})u(\mathbf{s})dB(\mathbf{s})-\int_B U^E(\mathbf{s},\mathbf{x})t(\mathbf{s})dB(\mathbf{s}),\quad \mathbf{x}\in D\cup B, \tag{30}$$

$$2\pi t(\mathbf{x})=\int_B M^E(\mathbf{s},\mathbf{x})u(\mathbf{s})dB(\mathbf{s})-\int_B L^E(\mathbf{s},\mathbf{x})t(\mathbf{s})dB(\mathbf{s}),\quad \mathbf{x}\in D\cup B \tag{31}$$

and

$$0=\int_B T^I(\mathbf{s},\mathbf{x})u(\mathbf{s})dB(\mathbf{s})-\int_B U^I(\mathbf{s},\mathbf{x})t(\mathbf{s})dB(\mathbf{s}),\quad \mathbf{x}\in D^c\cup B, \tag{32}$$

$$0=\int_B M^I(\mathbf{s},\mathbf{x})u(\mathbf{s})dB(\mathbf{s})-\int_B L^I(\mathbf{s},\mathbf{x})t(\mathbf{s})dB(\mathbf{s}),\quad \mathbf{x}\in D^c\cup B \tag{33}$$

In Fig. 2, decomposition and superposition techniques are employed to solve the porous cylinder problems. The solution of each cylinder part in Fig. 2(c) is derived from Eq. (28) by moving the point in the fluid domain to boundary. The exterior problem as shown in Fig. 2(e) is solved using Eq. (32) after moving the point $\mathbf{x}$ in the cylinder to boundary. After obtaining the boundary unknowns, Eq. (30) is used for the radiation field by collocating the point in the fluid domain. By combining with the incident wave, we can obtain the total field.

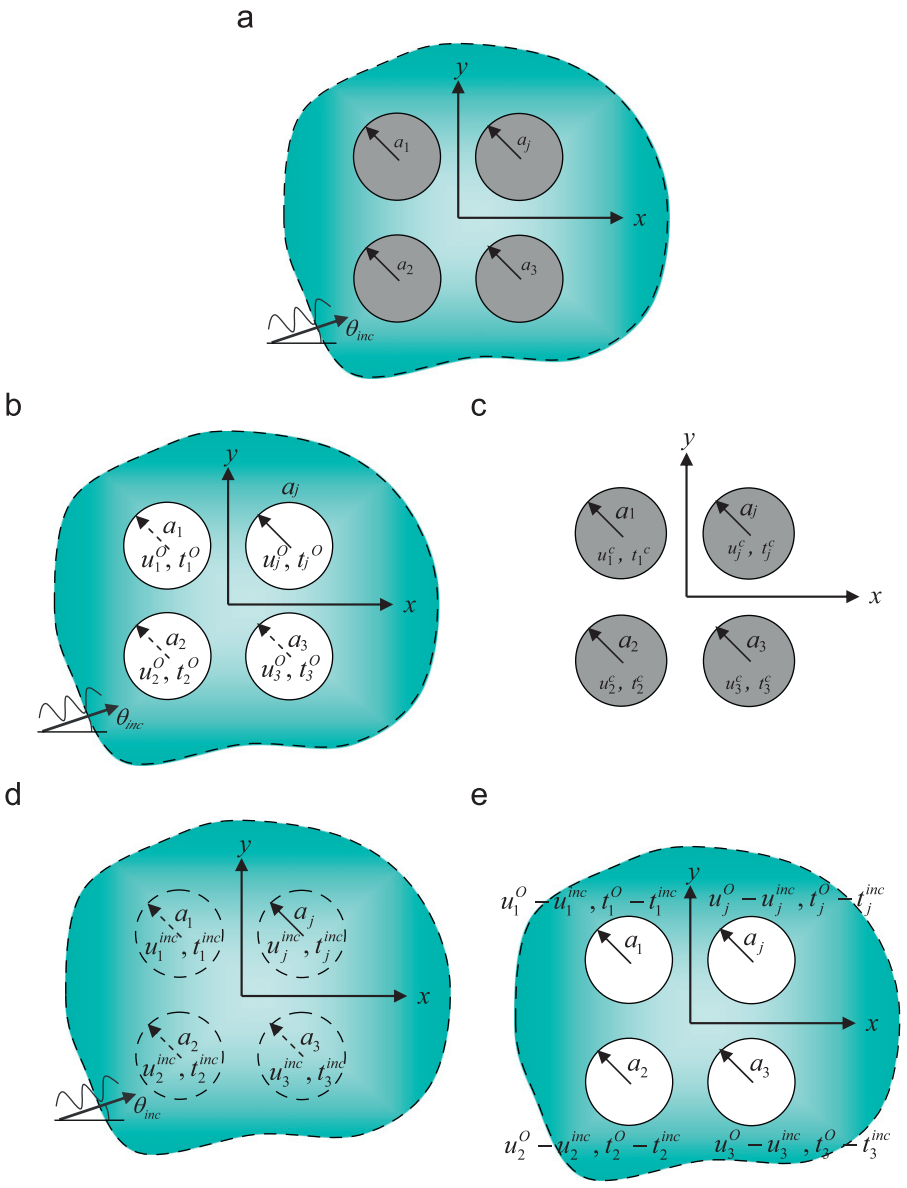

Fig. 2. (a) A water wave problem with multiple circular cylinders, (b) an infinite domain with multiple cylinders subject to incident water wave, (c) an interior Helmholtz problem for each circular cylinder, (d) an infinite domain subject to the incident water wave, and (e) an exterior Helmholtz problem in an infinite domain.

2.4. Expansions of fundamental solution and boundary density

Based on the separable property, the kernel function $U(\mathbf{s},\mathbf{x})$can be expanded into degenerate form by separating the source point and field point in the polar coordinates. Since degenerate kernels can describe the fundamental solutions in two regions (interior and exterior domains), the BIE for the domain point in Eqs. (26) and (27) and Eqs. (30) and (31) and the null-field BIE in Eqs. (28) and (29) and Eqs. (32) and (33), can be directly employed for the real boundary point. By using the polar coordinates, we can express $\mathbf{x}=(\rho,\phi)$ and $\mathbf{s}=(R,\theta)$. The four kernels U, T, L and M can be expressed in terms of separable kernels (Chen et al., 2009) as shown below:

$$U(\mathbf{s},\mathbf{x})=\begin{cases} U^I(R,\theta;\rho,\phi)=\dfrac{-\pi i}{2}\displaystyle\sum_{m=0}^{\infty}\varepsilon_m J_m(k\rho)H_m^{(1)}(kR)\cos(m(\theta-\phi)), & R\geq\rho,\\ U^E(R,\theta;\rho,\phi)=\dfrac{-\pi i}{2}\displaystyle\sum_{m=0}^{\infty}\varepsilon_m H_m^{(1)}(k\rho)J_m(kR)\cos(m(\theta-\phi)), & R<\rho, \end{cases} \tag{34}$$

$$T(\mathbf{s},\mathbf{x})=\begin{cases} T^I(R,\theta;\rho,\phi)=\dfrac{-\pi ki}{2}\displaystyle\sum_{m=0}^{\infty}\varepsilon_m J_m(k\rho)H_m^{(1)\prime}(kR)\cos(m(\theta-\phi)), & R>\rho,\\ T^E(R,\theta;\rho,\phi)=\dfrac{-\pi ki}{2}\displaystyle\sum_{m=0}^{\infty}\varepsilon_m H_m^{(1)}(k\rho)J_m'(kR)\cos(m(\theta-\phi)), & R<\rho, \end{cases} \tag{35}$$

$$L(\mathbf{s},\mathbf{x})=\begin{cases} L^I(R,\theta;\rho,\phi)=\dfrac{-\pi ki}{2}\displaystyle\sum_{m=0}^{\infty}\varepsilon_m J_m'(k\rho)H_m^{(1)}(kR)\cos(m(\theta-\phi)), & R>\rho,\\ L^E(R,\theta;\rho,\phi)=\dfrac{-\pi ki}{2}\displaystyle\sum_{m=0}^{\infty}\varepsilon_m H_m^{(1)\prime}(k\rho)J_m(kR)\cos(m(\theta-\phi)), & R<\rho, \end{cases} \tag{36}$$

$$M(\mathbf{s},\mathbf{x})=\begin{cases} M^I(R,\theta;\rho,\phi)=\dfrac{-\pi k^2 i}{2}\displaystyle\sum_{m=0}^{\infty}\varepsilon_m J_m'H_m^{(1)\prime}(kR)\cos(m(\theta-\phi)), & R\geq\rho,\\ M^E(R,\theta;\rho,\phi)=\dfrac{-\pi k^2 i}{2}\displaystyle\sum_{m=0}^{\infty}\varepsilon_m H_m^{(1)\prime}(k\rho)J_m'(kR)\cos(m(\theta-\phi)), & R<\rho \end{cases} \tag{37}$$

where ε_m is the Neumann factor

$$\varepsilon_m = \begin{cases} 1, & m=0, \\ 2, & m=1, \quad 2, \cdots, \infty \end{cases} \tag{38}$$

Mathematically speaking, the expressions of fundamental solutions in Eqs. (34)–(37) are termed separable kernels which can expand the kernel to sums of products of function of the field point **x** alone and functions of the source point **s** alone,. If the finite sum of series is considered, the degenerate kernel is finite rank. As we shall see in the later sections, the theory of boundary integral equations with degenerate kernel is nothing more than the linear algebra. Since the potentials resulted from $T(\mathbf{s},\mathbf{x})$ and $L(\mathbf{s},\mathbf{x})$ are discontinuous across the boundary, the potentials of $T(\mathbf{s},\mathbf{x})$ and $L(\mathbf{s},\mathbf{x})$ for $R\to\rho^+$ and $R\to\rho^-$ are different. This is the reason why $R=\rho$ is not included in the expression for the degenerate kernels of $T(\mathbf{s},\mathbf{x})$ and $L(\mathbf{s},\mathbf{x})$ in Eqs. (35) and (36). The degenerate kernels simply serve as the means to evaluate regular integrals analytically and take the limits analytically. The reason is that integral equation for the domain point of Eq. (26) and the null-field integral equation of Eq. (28) yield the same algebraic equation when the limit is taken from the inside or from the outside of the region. Both limits represent the same algebraic equation that is an approximate counterpart of the boundary integral equation, that for the case of a smooth boundary has in the left-hand side term $\pi u(\mathbf{x})$ or $\pi t(\mathbf{x})$ rather than $2\pi u(\mathbf{x})$ or $2\pi t(\mathbf{x})$ for the domain point or 0 for the point outside the domain. Besides, the limiting case to the boundary is also addressed. The continuous and jump behavior across the boundary is well captured by the Wronskian property of the Bessel function J_m and Y_m bases

$$W(J_m(kR), \quad Y_m(kR)) = Y'_m(kR)J_m(kR) - Y_m(kR)J'_m(kR) = \frac{2}{\pi kR} \tag{39}$$

as shown below

$$\int_0^{2\pi} (T^I(\mathbf{s},\mathbf{x}) - T^E(\mathbf{s},\mathbf{x}))\cos(m\theta)Rd\theta = 2\pi\cos(m\phi), \quad \mathbf{x}\in B, \tag{40}$$

$$\int_0^{2\pi} (T^I(\mathbf{s},\mathbf{x}) - T^E(\mathbf{s},\mathbf{x}))\sin(m\theta)Rd\theta = 2\pi\sin(m\phi), \quad \mathbf{x}\in B \tag{41}$$

After employing Eqs. (40) and (41), Eqs. (30) and (32) yield the same linear algebraic equation when **x** is exactly located the boundary from the domain or the complementary domain. A proof for the Laplace case can be found by Chen et al. (2006).

In order to fully utilize the geometry of circular boundary, the boundary potential $u(\mathbf{s})$ and its normal flux $t(\mathbf{s})$ can be approximated by employing the Fourier series. Therefore, we obtain

$$u(\mathbf{s}) = a_0 + \sum_{n=1}^{\infty} (a_n\cos n\theta + b_n\sin n\theta), \quad \mathbf{s}\in B, \tag{42}$$

$$t(\mathbf{s}) = p_0 + \sum_{n=1}^{\infty} (p_n\cos n\theta + q_n\sin n\theta), \quad \mathbf{s}\in B \tag{43}$$

where a_0, a_n, b_n, p_0, p_n and q_n are the Fourier coefficients and θ is the polar angle which is equally discretized. Eqs. (32) and (33) can be easily calculated by employing the orthogonal property of the Fourier series. In the real computation, only the finite M terms are used in the summation of Eqs. (42) and (43).

2.5. Adaptive observer system

To avoid using the addition theorem for translating the Bessel function, the adaptive observer system is adopted for pursuing the analytical boundary integrals. Since the boundary integral equations are frame indifferent, *i.e.,* rule of objectivity is obeyed. Adaptive observer system is chosen to fully employ the property of degenerate kernels. The "adaptive observer system" is one kind of the concept of "local coordinate". Fig. 3(a) shows the boundary integration for the circular boundaries. It is worthy of noting that the origin of the observer system can be adaptively located on the center of the corresponding circle under integration to fully utilize the geometry of circular boundary and orthogonal relations of the Fourier bases. Therefore, the origin of the observer system is not fixed to the circle under integration, but is adaptively changed according to the corresponding contour integration. We called this "adaptive observer system". The dummy variable in the integration on the circular boundary is just the angle (θ) instead of the radial coordinate (R). By using the adaptive observer system, all the boundary integrals can be determined analytically free of principal value.

2.6. Linear algebraic equation

After locating the null-field point x_k exactly on the kth circular boundary in Eq. (32) as shown in Fig. 3(a), we have

$$0 = \sum_{k=0}^{N} \int_{B_k} T^I(\mathbf{s},\mathbf{x})u(\mathbf{s})dB(\mathbf{s}) - \sum_{k=0}^{N} \int_{B_k} U^I(\mathbf{s},\mathbf{x})t(\mathbf{s})dB(\mathbf{s}), \quad \mathbf{x}\in D^c\cup B \tag{44}$$

where N is the number of circular cylinders and B_0 denotes the outer boundary for the bounded domain. In case of the infinite problem, B_0 becomes B_∞. The origin of observer system is adaptively chosen at the center of circular boundary under integration. The dummy variable in the circular integration is angle (θ) instead of radial coordinate (R). In the real computation, we select the collocation point on the real boundary and the integration path is counterclockwise for the outer circle. Otherwise, it is clockwise. For the integration path B_k, the kernels of $U(\mathbf{s},\mathbf{x})$and $T(\mathbf{s},\mathbf{x})$ are respectively expressed in terms of degenerate kernels of Eqs. (34) and (35) with respect to the observer origin at the center of

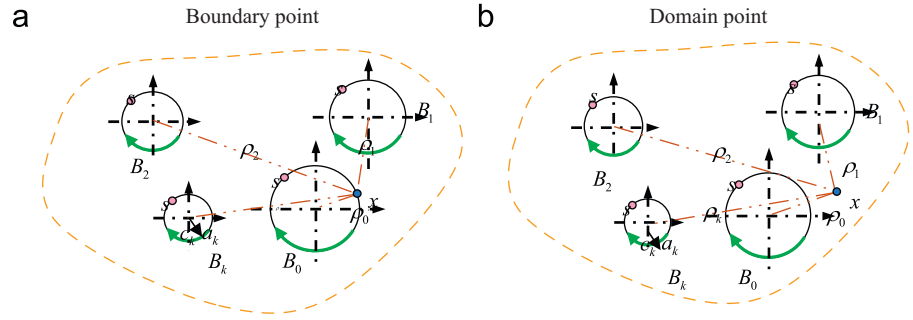

Fig. 3. An adaptive observer system (a) boundary point, and (b) domain point.

the corresponding path. The boundary densities of $u(\mathbf{s})$ and $t(\mathbf{s})$ are substituted by using the Fourier series of Eqs. (42) and (43), respectively. In the B_k integration, we set the origin of the observer system to collocate at the center c_k of B_k to fully utilize the degenerate kernel and the Fourier series. By moving the null-field point exactly on the real boundary B_k from outside of the domain D^c in the numerical implementation, a linear algebraic system is obtained.

For the exterior problem of infinite domain, we have

$$[\mathbf{U}^I]\{\mathbf{t}^O-\mathbf{t}^{\rm inc}\}=[\mathbf{T}^I]\{\mathbf{u}^O-\mathbf{u}^{\rm inc}\} \tag{45}$$

For the interior problem of each cylinder, we have

$$[\mathbf{U}^E]\{\mathbf{t}^C\}=[\mathbf{T}^E]\{\mathbf{u}^C\} \tag{46}$$

$[\mathbf{U}^I]$, $[\mathbf{T}^I]$, $[\mathbf{U}^E]$ and $[\mathbf{T}^E]$ are the influence matrices with a dimension of $N\times(2M+1)$ by $N\times(2M+1)$, $\{\mathbf{t}^O\}$, $\{\mathbf{t}^{inc}\}$, $\{\mathbf{u}^O\}$, $\{\mathbf{u}^{inc}\}$, $\{\mathbf{t}^C\}$ and $\{\mathbf{u}^C\}$ denote the column vectors of the Fourier coefficients with a dimension of $N\times(2M+1)$ by 1 in which those are defined as follows:

$$[U^I_{jk}]=\begin{bmatrix}\mathbf{U}^I_{00} & \mathbf{U}^I_{01} & \cdots & \mathbf{U}^I_{0N}\\ \mathbf{U}^I_{10} & \mathbf{U}^I_{11} & \cdots & \mathbf{U}^I_{1N}\\ \vdots & \vdots & \ddots & \vdots\\ \mathbf{U}^I_{N0} & \mathbf{U}^I_{N1} & \cdots & \mathbf{U}^I_{NN}\end{bmatrix}, \tag{47}$$

$$[T^I_{jk}]=\begin{bmatrix}\mathbf{T}^I_{00} & \mathbf{T}^I_{01} & \cdots & \mathbf{T}^I_{0N}\\ \mathbf{T}^I_{10} & \mathbf{T}^I_{11} & \cdots & \mathbf{T}^I_{1N}\\ \vdots & \vdots & \ddots & \vdots\\ \mathbf{T}^I_{N0} & \mathbf{T}^I_{N1} & \cdots & \mathbf{T}^I_{NN}\end{bmatrix}, \tag{48}$$

$$[U^E_{jk}]=\begin{bmatrix}\mathbf{U}^E_{00} & 0 & \cdots & 0\\ 0 & \mathbf{U}^E_{11} & \cdots & 0\\ \vdots & \vdots & \ddots & \vdots\\ 0 & 0 & \cdots & \mathbf{U}^E_{NN}\end{bmatrix}, \tag{49}$$

$$[T^E_{jk}]=\begin{bmatrix}\mathbf{T}^E_{00} & 0 & \cdots & 0\\ 0 & \mathbf{T}^E_{11} & \cdots & 0\\ \vdots & \vdots & \ddots & \vdots\\ 0 & 0 & \cdots & \mathbf{T}^E_{NN}\end{bmatrix}, \tag{50}$$

$$\{\mathbf{u}^O\}=\begin{Bmatrix}\mathbf{u}^O_0\\ \mathbf{u}^O_1\\ \vdots\\ \mathbf{u}^O_N\end{Bmatrix},\quad \{\mathbf{u}^{\rm inc}\}=\begin{Bmatrix}\mathbf{u}^{\rm inc}_0\\ \mathbf{u}^{\rm inc}_1\\ \vdots\\ \mathbf{u}^{\rm inc}_N\end{Bmatrix},\quad \{\mathbf{t}^O\}=\begin{Bmatrix}\mathbf{t}^O_0\\ \mathbf{t}^O_1\\ \vdots\\ \mathbf{t}^O_N\end{Bmatrix},\quad \{\mathbf{t}^{\rm inc}\}=\begin{Bmatrix}\mathbf{t}^{\rm inc}_0\\ \mathbf{t}^{\rm inc}_1\\ \vdots\\ \mathbf{t}^{\rm inc}_N\end{Bmatrix}, \tag{51}$$

$$\{\mathbf{u}^I\}=\begin{Bmatrix}\mathbf{u}^C_0\\ \mathbf{u}^C_1\\ \vdots\\ \mathbf{u}^C_N\end{Bmatrix},\quad \{\mathbf{t}^I\}=\begin{Bmatrix}\mathbf{t}^C_0\\ \mathbf{t}^C_1\\ \vdots\\ \mathbf{t}^C_N\end{Bmatrix} \tag{52}$$

the first subscript j (j=0, 1, 2, …, N) in $[\mathbf{U}^E]$, $[\mathbf{T}^E]$, $[\mathbf{U}^I]$ and $[\mathbf{T}^I]$ denotes the index of the jth circular boundary, where the collocation point is located and the second subscript k (k=0, 1, 2, …, N) denotes the index of the kth circular boundary when integrating on each boundary data $\{\mathbf{t}^O-\mathbf{t}^{inc}\}$, $\{\mathbf{u}^O-\mathbf{u}^{\rm inc}\}$ in Fig. 2(e), $\{\mathbf{t}^C\}$ and $\{\mathbf{u}^C\}$in Fig. 2(c), N is the number of circular cylinders in the domain and the number M indicates the truncated terms of the Fourier series. It is noted that $\{\mathbf{u}^{inc}\}$ and $\{\mathbf{t}^{inc}\}$ in Fig. 2(d) are the potential and flux due to the incident wave. The coefficient matrix of the linear algebraic system is partitioned into blocks, and each off-diagonal block corresponds to the influence matrices between two different circular boundaries. The diagonal blocks are the influence matrices due to itself in each individual circle. After uniformly collocating the point along the kth circular boundary, the submatrix can be written as

$$[\mathbf{U}_{jk}]=\begin{bmatrix}\mathbf{U}^{0c}_{jk}(\phi_1) & \mathbf{U}^{1c}_{jk}(\phi_1) & \mathbf{U}^{1s}_{jk}(\phi_1) & \cdots & \mathbf{U}^{Mc}_{jk}(\phi_1) & \mathbf{U}^{Ms}_{jk}(\phi_1)\\ \mathbf{U}^{0c}_{jk}(\phi_2) & \mathbf{U}^{1c}_{jk}(\phi_2) & \mathbf{U}^{1s}_{jk}(\phi_2) & \cdots & \mathbf{U}^{Mc}_{jk}(\phi_2) & \mathbf{U}^{Ms}_{jk}(\phi_2)\\ \mathbf{U}^{0c}_{jk}(\phi_3) & \mathbf{U}^{1c}_{jk}(\phi_3) & \mathbf{U}^{1s}_{jk}(\phi_3) & \cdots & \mathbf{U}^{Mc}_{jk}(\phi_3) & \mathbf{U}^{Ms}_{jk}(\phi_3)\\ \vdots & \vdots & \vdots & & \vdots & \vdots\\ \mathbf{U}^{0c}_{jk}(\phi_{2M}) & \mathbf{U}^{1c}_{jk}(\phi_{2M}) & \mathbf{U}^{1s}_{jk}(\phi_{2M}) & \cdots & \mathbf{U}^{Mc}_{jk}(\phi_{2M}) & \mathbf{U}^{Ms}_{jk}(\phi_{2M})\\ \mathbf{U}^{0c}_{jk}(\phi_{2M+1}) & \mathbf{U}^{1c}_{jk}(\phi_{2M+1}) & \mathbf{U}^{1s}_{jk}(\phi_{2M+1}) & \cdots & \mathbf{U}^{Mc}_{jk}(\phi_{2M+1}) & \mathbf{U}^{Ms}_{jk}(\phi_{2M+1})\end{bmatrix}, \tag{53}$$

$$[\mathbf{T}_{jk}]=\begin{bmatrix}\mathbf{T}^{0c}_{jk}(\phi_1) & \mathbf{T}^{1c}_{jk}(\phi_1) & \mathbf{T}^{1s}_{jk}(\phi_1) & \cdots & \mathbf{T}^{Mc}_{jk}(\phi_1) & \mathbf{T}^{Ms}_{jk}(\phi_1)\\ \mathbf{T}^{0c}_{jk}(\phi_2) & \mathbf{T}^{1c}_{jk}(\phi_2) & \mathbf{T}^{1s}_{jk}(\phi_2) & \cdots & \mathbf{T}^{Mc}_{jk}(\phi_2) & \mathbf{T}^{Ms}_{jk}(\phi_2)\\ \mathbf{T}^{0c}_{jk}(\phi_3) & \mathbf{T}^{1c}_{jk}(\phi_3) & \mathbf{T}^{1s}_{jk}(\phi_3) & \cdots & \mathbf{T}^{Lc}_{jk}(\phi_3) & \mathbf{T}^{Ms}_{jk}(\phi_3)\\ \vdots & \vdots & \vdots & \ddots & \vdots & \vdots\\ \mathbf{T}^{0c}_{jk}(\phi_{2M}) & \mathbf{T}^{1c}_{jk}(\phi_{2M}) & \mathbf{T}^{1s}_{jk}(\phi_{2M}) & \cdots & \mathbf{T}^{Mc}_{jk}(\phi_{2M}) & \mathbf{T}^{Ms}_{jk}(\phi_{2M})\\ \mathbf{T}^{0c}_{jk}(\phi_{2M+1}) & \mathbf{T}^{1c}_{jk}(\phi_{2M+1}) & \mathbf{T}^{1s}_{jk}(\phi_{2M+1}) & \cdots & \mathbf{T}^{Mc}_{jk}(\phi_{2M+1}) & \mathbf{T}^{Ms}_{jk}(\phi_{2M+1})\end{bmatrix}, \tag{54}$$

It is noted that the superscript 0s in Eq. (53) disappears since $\sin(0\theta)=0$, and the element of $[\mathbf{U}_{jk}]$ and $[\mathbf{T}_{jk}]$ are defined as

$$\mathbf{U}^{nc}_{jk}=\int_{B_k}\mathbf{U}(\mathbf{s}_k,\mathbf{x}_m)\cos(n\theta_k)R_k d\theta_k \tag{55}$$

$$\mathbf{U}^{ns}_{jk}=\int_{B_k}\mathbf{U}(\mathbf{s}_k,\mathbf{x}_m)\sin(n\theta_k)R_k d\theta_k \tag{56}$$

$$\mathbf{T}^{nc}_{jk}=\int_{B_k}\mathbf{T}(\mathbf{s}_k,\mathbf{x}_m)\cos(n\theta_k)R_k d\theta_k \tag{57}$$

$$\mathbf{T}^{ns}_{jk}=\int_{B_k}\mathbf{T}(\mathbf{s}_k,\mathbf{x}_m)\sin(n\theta_k)R_k d\theta_k \tag{58}$$

where n=1,2,…,M, ϕ_m(m=1,2,…,2M+1) is the polar angle of the collocating point $\mathbf{x}_m$ along the boundary. By assembling matrices in Eqs. (11), (45) and (46), we have

$$\begin{bmatrix}\mathbf{T}^I & -\mathbf{U}^I & 0 & 0\\ 0 & 0 & \mathbf{T}^E & -\mathbf{U}^E\\ 0 & +\mathbf{I} & 0 & -\mathbf{I}\\ {\rm ikG} & 0 & -{\rm ikG} & \mathbf{I}\end{bmatrix}\begin{Bmatrix}\mathbf{u}^O\\ \mathbf{t}^O\\ \mathbf{u}^C\\ \mathbf{t}^C\end{Bmatrix}=\begin{bmatrix}\mathbf{W}_{\rm inc}\\ 0\\ 0\\ 0\end{bmatrix} \tag{59}$$

where the matrix $[I]$ is an identity matrix and $\mathbf{W}_{\rm inc}=[\mathbf{T}^I]\{\mathbf{u}^{\rm inc}\}-[\mathbf{U}^I]\{\mathbf{t}^{\rm inc}\}$ is the forcing term. After obtaining the unknown Fourier coefficients, the origin of observer system is set at c_j in the B_j integration as shown in Fig. 3(b) to obtain the interior potential by employing Eq. (32).

2.7. Perturbation of ordered cylinder arrangements

An arrangement of four and sixteen cylinders according to a regular three-rows disposition is shown in Fig. 4(a) and (b). For the purpose of disturbing the regular arrangement, a perturbation of disposition is given. The displacement of each cylinder center apart from its original periodical position is defined as follows

$$\begin{aligned}\Delta x_j&=\gamma_j p\tau\cos(2\pi\gamma_j),\\ \Delta y_j&=\gamma_j p\tau\sin(2\pi\gamma_j)\end{aligned} \tag{60}$$

where γ_j is a random variable in the range of [0,1], the maximum permissible displacement p is equal to d–a and τ is a global disorder parameter. The distance between the two centers of identical cylinders is 2b where the radii of cylinders are a.

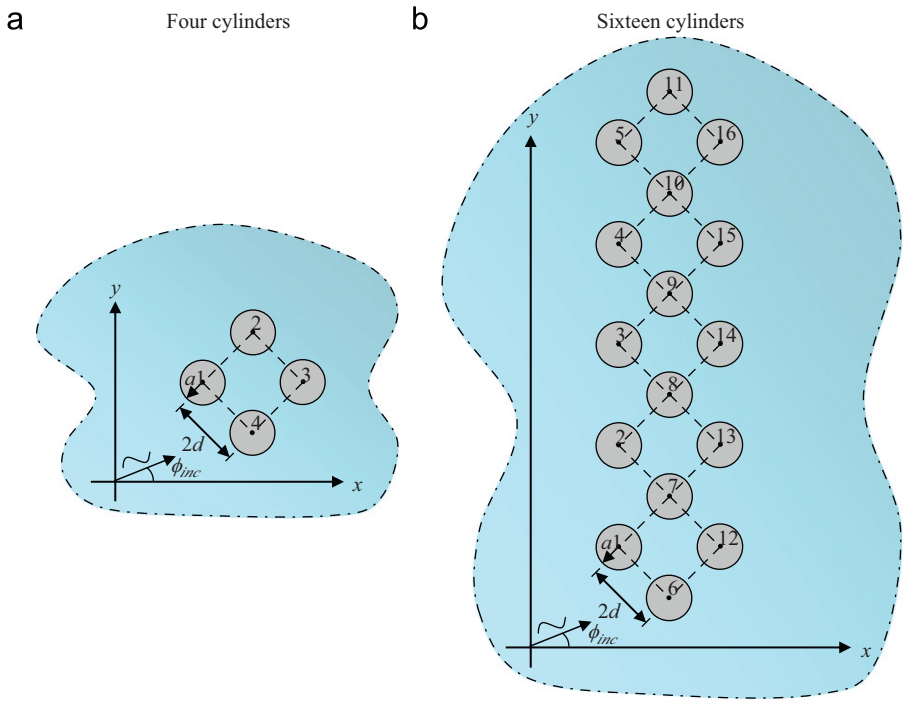

Fig. 4. Configuration of (a) four cylinders and (b) sixteen cylinders.

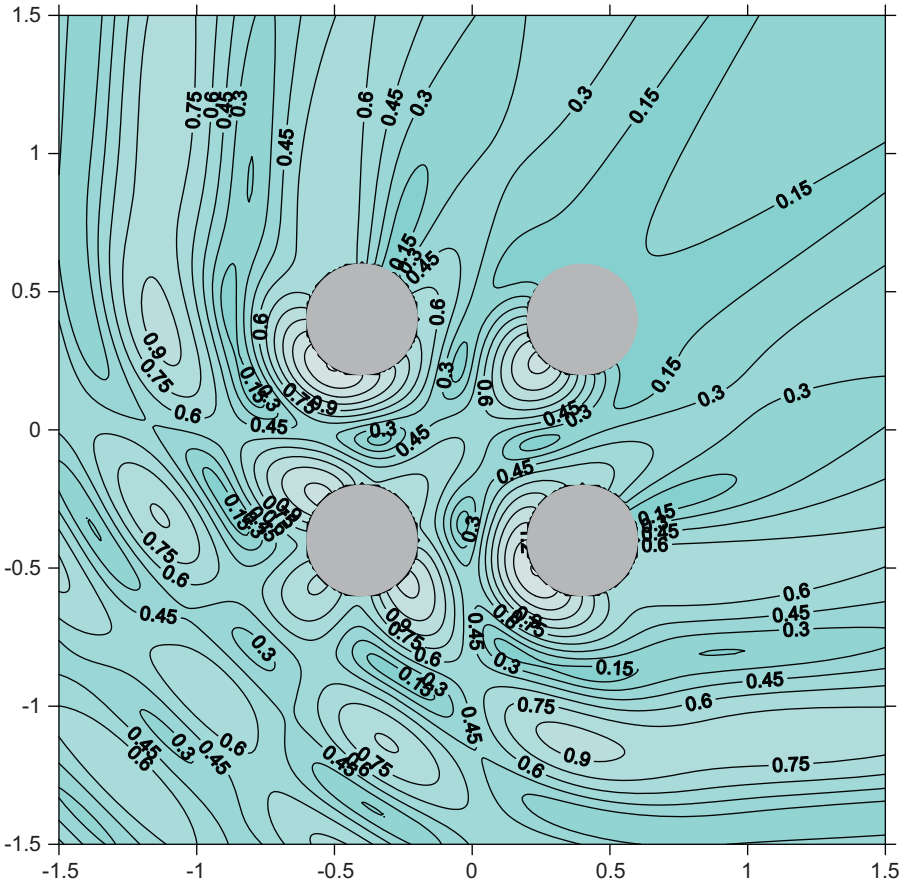

Fig. 5. Contour plots of free-surface elevation of the four impermeable cylinders. (G=0.0, θ_{inc}=45°, h/a=5, d/a=2 and $ka=\pi/2$).

3. Illustrative examples

3.1. Case 1: Four cylinders

For the 45° of incident wave to impermeable cylinders as shown in Fig. 4(a), the null-field BIEM is employed to calculate the free-surface elevation as shown in Fig. 5. To consider the porous effect ($G=1$), the contour plot of the free-surface elevation is shown in Fig. 6. After comparing Fig. 6 with Fig. 5, it is found that the elevation of free-surface becomes smaller when the porous effect ($G=1$) is considered. In Williams and Li's article, the elevation of free-surface is shown in the form of 3D plot, but our result shows in the form of contour plot. We could not compare our results and their ones directly. In Chen's thesis (2004), his results were compared well with those of Williams and Li. Chen also plotted the contour of free-surface elevation. After comparing with Chen's result, good agreements are made.

3.2. Case 2: Sixteen cylinders

For the sixteen cylinders composed by five sets, contour plots of the free-surface elevation are our main concern.

(a) *Without disorder and porosity*:
A trapped mode also appears for the same wave number of $k=4.08482$ by Chen et al. (2009) as the case of sixteen cylinders in Fig. 7 using our approach and compared well with those of Duclos and Clèment's method (2004). The maximum wave amplitude is predicted to be about 150 times by using both approaches. Fig. 8 shows the force experienced by cylinder No. 3 of the linear array in Fig. 4(b) and cylinder 1 (see Fig. 4(a)) of the circular cylinders by using our approach and is compared well with the result of Duclos and Clèment's method (2004).

(b) *Effect of disorder* (*impermeable case*):
As shown in Fig. 7, original state without disorder and porous effect is considered. Here, the effect of disorder is considered. Following the definition of disorder parameter τ, two random cases of $\tau=0.1$ were reported by Duclos and Clèment (2004).

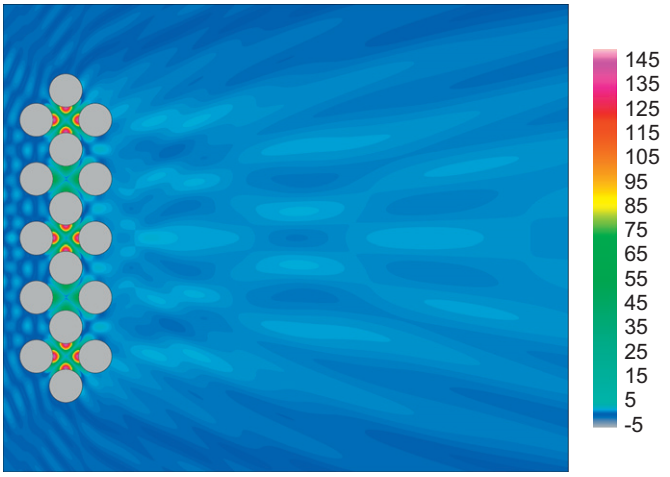

Fig. 7. Near-trapped mode for the ordered pile array at $ka=4.08482$ ($a/d=0.8$, $G=0.0$, $M=20$, and $\tau=0.0$).

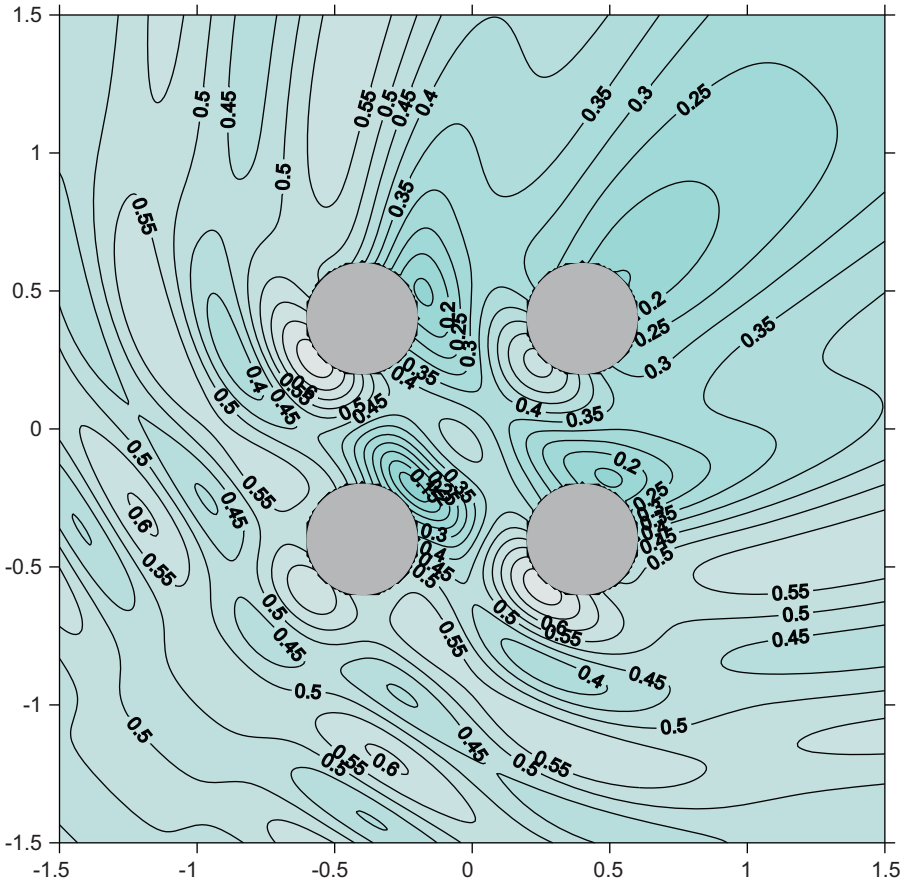

Fig. 6. Contour plots of free-surface elevation of the four porous cylinders ($G=1.0$, $\theta_{inc}=45°$, $h/a=5$, $d/a=2$ and $ka=\pi/2$).

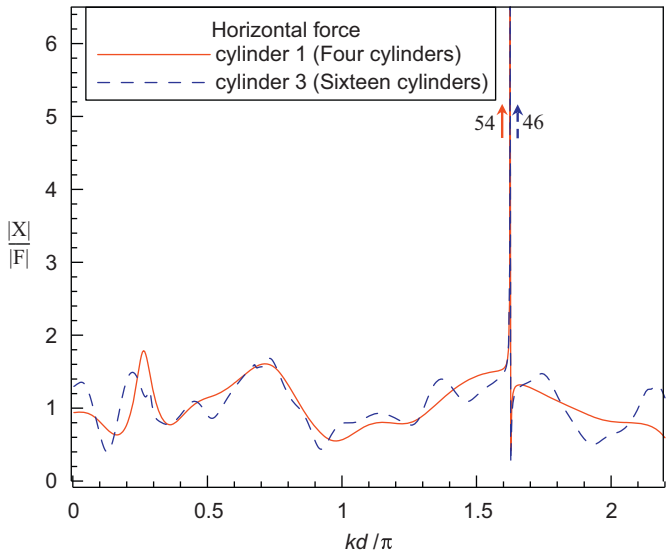

Fig. 8. Horizontal force on the corresponding cylinder of the ordered pile array. ($kd/\pi=1.625293$, $a/d=0.8$, $M=20$, and $\tau=0.0$).

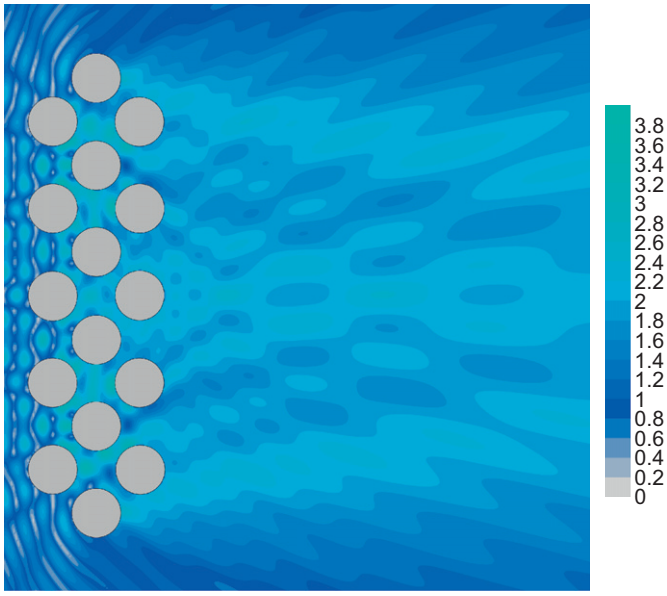

Fig. 9. Suppression of near-trapped modes by using disorder. ($a/d=0.8$ and $M=20$).

The appearance of the trapped mode is dramatically suppressed. To test the accuracy of our approach for the disorder effect, Fig. 9 shows that the contour plot of the trapped mode is effectively suppressed for $\tau=0.1$.

(c) *Effect of porosity*

To verify the effect of porous parameter on the trapped mode of sixteen cylinders, Figs. 7 and 10 show the contour plot of free-surface elevation. The maximum value of 150 reduces to 75 due to the porous parameter of $G=1.0$. This result agrees with Chwang's result that the resultant force decreases as the G value becomes larger.

(d) *Effect of porous parameter and disorder together*

To verify both the effects of disorder and porosity, a sixteen cylinders example is demonstrated here. Fig. 7 shows the contour of the free-surface elevation without disorder and porosity. By considering the perturbation parameter $\tau=0.1$, the maximum value of free-surface elevation reduces dramatically to 3.90 from the original value of 150 in Fig. 9. By only considering the porous cylinder without disorder, the maximum value is deduced to half as shown in Fig. 10 in comparison with 150 in Fig. 7. If the perturbation parameter and porosity are simultaneously considered, the maximum value of free-surface elevation reduces to 2.70 in Fig. 11. It indicates that disorder dominates the maximum free-surface elevation.

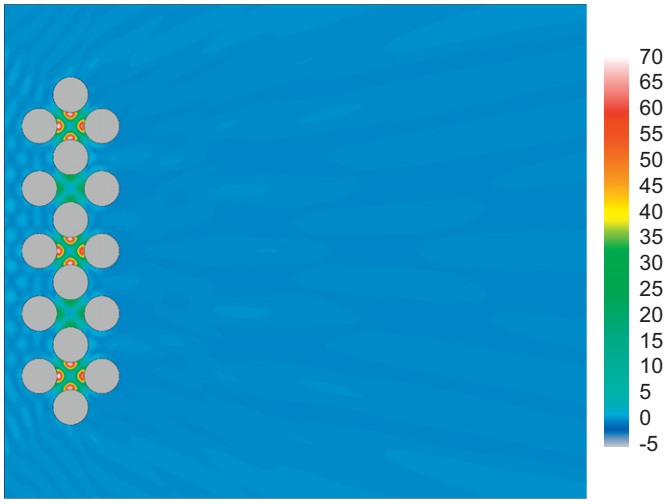

Fig. 10. Contour plot of the maximum free-surface elevation amplitude for porous cylinders ($a/d=0.8$, $G=1.0$, $\tau=0$, and $M=20$).

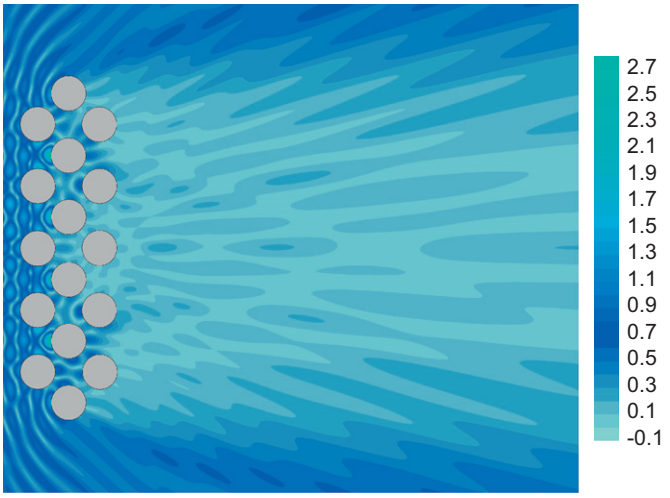

Fig. 11. Contour plot of the maximum free-surface elevation amplitude for the disorder and porous cylinders ($a/d=0.8$, $G=1.0$, $\tau=0.1$, and $M=20$).

4. Conclusions

In this paper, not only a systematic approach was employed to investigate the water wave interaction with arrays of surface-piercing porous cylinders, but also the effect of porous parameter and disorder on the force in case of trapped modes was also examined. The case of impermeable cylinder case can be treated as a special case with $G=0$. The addition theorem or so-called the degenerate kernel is adopted in the null-field integral formulation. Therefore, the singular integrals using bump integrals for principal values can be avoided. Numerical results including the free-surface elevation and resultant forces on each cylinder have been presented to illustrate the effect of porous and disorder parameter on the force in case of trapped modes. It is found that the disorder has

more influence to suppress the occurrence of near-trapped modes than the porosity. Good agreements are observed after comparing with the results obtained in the literature.

References

Au, M.C., Brebbia, C.A., 1983. Diffraction of water waves for vertical cylinders using boundary elements. Appl. Math. Model. 7, 106–114.

Chen, J.T., Chen, K.H., Chen, I.L., Liu, L.W., 2003. A new concept of modal participation factor for numerical instability in the dual BEM for exterior acoustics. Mech. Res. Commun. 26 (2), 161–174.

Chen, J.T., Shen, W.C., Wu, A.C., 2006. Null-field integral equations for stress field around circular holes under antiplane shear. Eng. Anal. Bound. Elem. 30, 205–217.

Chen, J.T., Lee, Y.T., Lin, Y.J., 2009. Interaction of water waves with arbitrary vertical cylinders using null-field integral equations. Appl. Ocean Res. 31 (2), 101–110.

Chen, Y.H., 2004. Wave-induced oscillations in harbors by permeable arc breakwaters, Master Thesis, National Taiwan Ocean University, Keelung, Taiwan.

Chwang, A.T., 1983. A porous wavemaker theory. J. Fluid Mech. 132, 395–406.

Duclos, G., Clèment, A.H., 2004. Wave propagation through arrays of unevenly spaced vertical piles. Ocean Eng. 31 (13), 1655–1668.

Eatock Taylor, R., Hung, S.M., 1985. Wave drift enhancement effect in multi column structures. Appl. Ocean Res. 7 (3), 128–137.

Evans, D.V., Porter, R., 1997. Near-trapping of waves by circular arrays of vertical cylinders. Appl. Ocean Res. 19, 83–99.

Evans, D.V., Porter, R., 1999. Trapping and near-trapping by arrays of cylinders in waves. J. Eng. Math. 35, 149–179.

Linton, C.M., Evans, D.V., 1990. The interaction of waves with arrays of vertical circular cylinders. J. Fluid Mech. 215, 549–569.

Maniar, H.D., Newman, J.N., 1997. Wave diffraction by a long array of cylinders. J. Fluid Mech. 339, 309–330.

MacCamy, R.C., Fuchs, R.A., 1954. Wave force on piles: A diffraction theory. Technical Memorandum No. 69, US Army Coastal Engineering Research Center (formerly Beach Erosion Board).

McIver, R., Evans, D.V., 1984. Approximation of wave forces on cylinder arrays. Appl. Ocean Res. 6 (2), 101–107.

Spring, B.H., Monkmeyer, P.L., 1974. Interaction of Plane Waves with Vertical Cylinders. In: Proceeding of 14th International Conference on Coastal Engineering, pp. 1828–1845.

Twersky, V., 1952. Multiple scattering of radiation by an arbitrary configuration of parallel cylinders. J. Acoust. Soc. Am. 24, 42–46.

Twu, S.W., Lin, D.T., 1991. On a highly effective wave absorber. Coastal Eng. 15, 389–405.

Williams, A.N., Li, W., 2000. Water wave interaction with an array of bottom-mounted surface-piercing porous cylinders. Ocean Eng. 27, 841–866.

Zhu, S.P., Moule, G., 1996. An efficient numerical calculation of water loads on an array of vertical cylinders. Appl. Math. Model. 20, 26–33.